J|A|C|S ARTICLES

Published on Web 05/11/2010

# Nanoscale Structure, Composition, and Charge Transport Analysis of Transparent Conducting Oxide Nanowires Written by Focused Ion Beam Implantation

Norma E. Sosa,[†] Christopher Chen,[†] Jun Liu,[‡] Sujing Xie,[†] Tobin J. Marks,*[,†,‡] and Mark C. Hersam*[,†,‡]

*Department of Materials Science and Engineering and the Materials Research Center, Northwestern University, 2220 Campus Drive, Evanston, Illinois 60208-3108, and Department of Chemistry and the Materials Research Center, Northwestern University, 2145 Sheridan Road, Evanston, Illinois 60208-3113*

Received October 30, 2009; E-mail: m-hersam@northwestern.edu; t-marks@northwestern.edu

***Abstract:*** Realizing optically transparent functional circuitry continues to fuel scientific and technological interest in transparent conducting oxides (TCOs). However, precise means for creating transparent interconnects for device-to-device integration has remained elusive. Here we report on the chemical, microstructural, and electronic properties of transparent conducting oxide nanowires (Ga-doped $In_2O_3$) created by direct-write focused ion beam ($Ga^+$) implantation within an insulating oxide substrate ($In_2O_3$). First, methodology for preparing TEM-ready samples is presented that enables detailed TEM-based analysis of individual nanowires. Differences in diffraction features between doped and undoped oxide regions, accompanied by RTA results, support a model in which oxygen vacancies and amorphization comprise the predominant doping/carrier creation mechanism. The same isolated nanowires are then subjected to chemical profiling, providing quantitative information on the lateral Ga doping dimensions, which are in good agreement with conductive AFM images. Furthermore, spatially selective nanoscale EELS spectroscopy provides additional evidence for changes in the oxygen site chemical environment in the FIB-processed/doped $In_2O_3$, and for negligible changes in the surrounding non-FIB-processed/undoped oxide. The nanowires exhibit ohmic electrical behavior and with an average estimated conductivity of 1600−3600 S $cm^{-1}$, similar to macroscale Ga-doped $In_2O_3$ films grown by conventional processes.

## 1. Introduction

The implementation of transparent oxides as the basis for all-transparent electronic circuitry has attracted great interest as a driver in both scientific and consumer electronics.[1−8] The required transparent oxide (TO) materials suite must necessarily include transparent conducting oxides (TCOs), transparent oxide semiconductors (TOSs, which are not degenerately doped in contrast to their TCO counterparts), and transparent oxide insulators (TOIs). This range of electrical properties, combined with optical transparency, renders this materials family uniquely suitable to serve as the foundation for all-oxide electronics.[9,10] The reason why TOs[5,7,9] can play a primary role in this emerging field is that, when degenerately doped, they exhibit near-metallic conductivities while maintaining 3.6−3.8 eV bandgaps.[11]

Transparent conducting oxides[12−14] were first discovered by Badeker, who observed that oxidized metallic Cd films are both transparent and electrically conducting.[15] Although CdO was the first TCO discovered, it is tin-doped indium oxide, (ITO) that is the most widely used in commercial optoelectronics. More recently[10,16] research turned to multication TCOs such as Gd-doped $InO_x$ and F-doped $In_2O_3$;[15] Al-, In-, B-, and Ga-doped ZnO;[6,15] and Sc-, In-, and Zn-doped CdO.[17−19] Ternary systems are also being studied, including (Zn-In-Ga)-O, (Ga-In-Sn)-O, and (Cd-In-Sn)-O.[16] Applications of TCOs are diverse and include transparent anodes in optoelectronics,[15,20−23] heat mirrors for solar collectors,[24−26] electrodes and antireflection

[†] Department of Materials Science and Engineering and the Materials Research Center.

[‡] Department of Chemistry and the Materials Research Center.

(1) *Transparent Electronics*; Facchetti, A., Marks, T., Eds.; Wiley: West Sussex, 2010.
(2) Banerjee, A.; Chattopadhyay, K. *P-Type Transparent Semiconducting Delafossite CuA1O2+x Thin Film*; Nova Science Publishers: Hauppauge, 2008.
(3) Sun, Y. G.; Rogers, J. A. *Adv. Mater.* **2007**, *19*, 1897.
(4) Song, K.; Kim, D.; Li, X. S.; Jun, T.; Jeong, Y.; Moon, J. *J. Mater. Chem.* **2009**, *19*, 8881.
(5) Kagan, C.; Andry, P. *Thin-Film Transistors*; CRC Press: New York, 2003.
(6) Fortunato, E.; Barquinha, P.; Pimentel, A.; Goncalves, A.; Marques, A.; Pereira, L.; Martins, R. *Thin Solid Films* **2005**, *487*, 205.
(7) Wager, J. F. *Science* **2003**, *300*, 1245.
(8) Nomura, K.; Ohta, H.; Takagi, A.; Kamiya, T.; Hirano, M.; Hosono, H. *Nature* **2004**, *432*, 488.
(9) Nomura, K.; Ohta, H.; Ueda, K.; Kamiya, T.; Hirano, M.; Hosono, H. *Science* **2003**, *300*, 1269.
(10) Kamiya, T.; Hiramatsu, H.; Nomura, K.; Hosono, H. *J. Electroceram.* **2006**, *17*, 267.
(11) Weiher, R. L.; Ley, R. P. *J. Appl. Phys.* **1966**, *37*, 299.
(12) Burstein, E. *Phys. Rev.* **1953**, 632.
(13) Tennenbaum, M.; Briggs, B. H. *Phys. Rev.* **1953**, *91*, 1591.
(14) Gordon, R. G. *Mater. Res. Soc. Bull.* **2000**, 52.
(15) Lewis, B. G.; Paine, D. C. *Mater. Res. Soc. Bull.* **2000**, 22.
(16) Freeman, A. J.; Poeppelmeier, K. R.; Mason, T. O.; Chang, R. P. H.; Marks, T. J. *Mater. Res. Soc. Bull.* **2000**, *25*, 45.

  

coatings in photovoltaics,[25,27−29] photodetectors,[28,30] flat panel and liquid crystal displays,[31] deicers, and IR-reflective coatings for architectural windows to reduce heating and cooling costs.[32,33]

The possibility of realizing truly "invisible electronics"[1,3] is promising since efficient transistor function utilizing all-transparent oxide active materials[9,28,34,35] has recently been demonstrated. Note, however, that in addition to transistors, transparent electronic integrated circuits will require transparent interconnects at or near the nanoscale. To address this need, patterning of TCO films via chemical/physical means has been reported,[36−40] specifically by subtractive wet etching through a resist mask.[40] While this offers large-scale parallel processing of transparent features, it is limited by poor control of the etching process, which depends on local microstructure, in turn limiting pattern resolution to a few hundred nanometers. Another means of creating nanoscale wires in predetermined patterns, although not demonstrated for TCOs, is using 35−100 keV ion beams (e.g., $B^+$, $O^+$, $P^+$, or $As^+$ beams) at $5 \times 10^{14}-10^{16}$ ions $cm^{-2}$ to locally decompose thin metal−organic blanket films. While this can create highly conductive 250 nm tall metallic structures with linewidths of ∼330 nm,[41,42] these structures are at most optically translucent at the densities necessary for integration. Thus, there remains a need for precisely positioned transparent conductive nanowires. To this end, a versatile means to create nanoscale, optically transparent, electrically conducting features on highly insulating host films would be highly desirable.

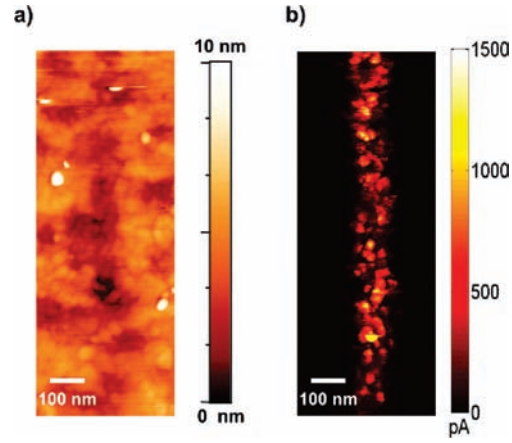


***Figure 1.*** Conductive AFM image of a single FIB patterned nanowire. (a) Topography and (b) current map for a nanowire written with $\sim 9 \times 10^{16}$ ions $cm^{-2}$ using a 5 kV beam energy at 1.5 pA beam current. Note that clusters of domain-like regions of higher conductance comprise the nanowires created by the implantation process. The average electrically active width of these nanowires is 100 nm.

In a preliminary communication,[43] we reported focused ion beam (FIB) fabrication of nanoscale TCO wires in $In_2O_3$ as judged by AFM imaging and SIMS depth-profiling.[43] The wire dimensions achieved were ≤160 nm wide and nominally ∼7 nm deep, with user-defined lengths (Figure 1). Importantly, state-of-the-art FIB processing implies full lithographic control, enabling the patterning of completely arbitrary shapes that are in principle limitless in length and connectivity. From the preliminary data, the "writing" mechanism was proposed to involve controlled FIB beam implantation of Ga dopant ions into the undoped host to create high electrical contrast between doped and undoped regions. Although this mechanism is qualitatively reasonable, numerous unanswered quantitative questions remained regarding the detailed chemical, structural, dimensional, and electrical properties of these wires, including the actual magnitude of the conductivity achieved and the carrier generation mechanism. Answering these key questions is the goal of the present study. This information is directly relevant to the chemical mechanism of charge carrier generation. To gain insight into the nanoscale compositional and structural changes, the nanowires are characterized using several transmission electron microscopy (TEM) techniques including bright-field (BF) and scanning TEM (STEM) imaging (Z-contrast imaging), as well as X-ray spectroscopy (EDXS) and electron energy loss spectroscopy (EELS). STEM mode information probes the Ga spatial distribution and provides oxygen site chemical information. In conjunction with parallel conductive AFM imaging, oxidative and reductive post rapid thermal anneal (RTA) experiments, nanodiffraction data, and distinctive EELS spectral features, it will be seen that definitive chemical and carrier generation mechanistic information is revealed. Finally, the FIB-derived nanowire electrical conductivity is quantified for the first time.

(17) Jin, S.; Yang, Y.; Medvedeva, J. E.; Ireland, J. R.; Metz, A. W.; Ni, J.; Kannewurf, C. R.; Freeman, A. J.; Marks, T. J. *J. Am. Chem. Soc.* **2004**, *126*, 13787.
(18) Wang, A.; Babcock, J. R.; Edleman, N. L.; Metz, A. W.; Lane, M. A.; Asahi, R.; Dravid, V. P.; Kannewurf, C. R.; Freeman, A. J.; Marks, T. J. *Proc. Nat. Acad. Sci. U.S.A.* **2001**, *98*, 7113.
(19) Zaoui, A.; Zaoui, M.; Kadmi, S.; Boukortt, A.; Bouhafs, B. *Mater. Chem. Phys.* **2010**, *120*, 98.
(20) Chaney, J. A.; Pehrsson, P. E. *Appl. Phys. Lett.* **2001**, *180*, 214.
(21) Christou, V.; Ethcells, M.; Renault, O.; Dobson, P. J.; Salata, O. V.; Beamson, G.; Edgell, R. G. *J. Appl. Phys.* **2000**, *88*, 5180.
(22) Park, Y.; Choong, V.; Gao, Y.; Hsieh, B. R.; Tang, C. W. *Appl. Phys. Lett.* **1996**, *68*, 2699.
(23) Purvis, K. L.; Lu, G.; Schwartz, J.; Bernasek, S. L. *J. Am. Chem. Soc.* **2000**, *122*, 1808.
(24) Brewer, S. H.; Franzen, S. *J. Alloys Compd.* **2002**, *338*, 73.
(25) Fan, J. C. C.; Goodenough, J. B. *J. Appl. Phys.* **1977**, *48*, 3524.
(26) Hamberg, I.; Granqvist, C. G. *J. Appl. Phys.* **1986**, *60*, R123.
(27) Nakao, T.; Nakada, T.; Nakayama, Y.; Miyatani, K.; Kimura, Y.; Saito, Y.; Kaito, C. *Thin Solid Films* **2000**, *370*, 155.
(28) Tahar, R. B. H.; Ban, T.; Ohya, Y.; Takahashi, Y. *J. Appl. Phys.* **1998**, *83*, 2631.
(29) Armstrong, N. R.; Veneman, P. A.; Ratcliff, E.; Placencia, D.; Brumbach, M. *Acc. Chem. Res.* **2009**, *42*, 1748.
(30) Azarian, A.; Zad, A. I.; Mahdavi, S. M.; Samadpoor, M. *Int. J. Nanotechnol.* **2009**, *6*, 997.
(31) Behdani, M.; Rastegar, A.; Keshmiri, S. H.; Missat, S. I.; Vlieg, E.; Rassing, T. *Appl. Phys. Lett.* **2002**, *80*, 4635.
(32) Jin, S.; Yang, Y.; Medvedeva, J. E.; Ireland, J. R.; Metz, A. W.; Ni, J.; Kannewurf, C. R.; Freeman, A. J.; Marks, T. J. *J. Am. Chem. Soc.* **2004**, *126*, 13787.
(33) Chopra, K. L.; Major, S.; Pandya, D. K. *Thin Solid Films* **1983**, *102*, 1.
(34) Song, K.; Kim, D.; Li, X.-S.; Jun, T.; Jeong, Y.; Moon, J. *J. Mater. Chem.* **2009**, *19*, 8881.
(35) Jackson, W. B.; Hoffman, R. L.; Herman, G. S. *Appl. Phys. Lett.* **2005**, 87.
(36) Yavas, O.; Takai, M. *Jpn. J. Appl. Phys., Part 1* **1999**, *38*, 7131.
(37) Molloy, J.; Maguire, P.; Laverty, S. J.; McLaughlin, J. A. *J. Electrochem. Soc.* **1995**, *142*, 4285.
(38) Chen, M. F.; Chen, Y. P.; Hsiao, W. T.; Gu, Z. P. *Thin Solid Films* **2007**, *515*, 8515.
(39) Chae, J.; Appasamy, S.; Jain, K. *Appl. Phys. Lett.* **2007**, 90.
(40) Breen, T. L.; Fryer, P. M.; Nunes, R. W.; Rothwell, M. E. *Langmuir* **2002**, *18*, 194.
(41) Catalan, A. B.; Mantese, J. V.; Hamdi, A. H.; Laugal, R. C. O.; Micheli, A. L. *Thin Solid Films* **1990**, *188*, 21.
(42) Hamdi, A. H.; Laugal, R. C. O.; Catalan, A. B.; Micheli, A. L.; Schubring, N. W. *Thin Solid Films* **1991**, *198*, 9.
(43) Sosa, N. E.; Liu, J.; Chen, C.; Marks, T. J.; Hersam, M. C. *Adv. Mater.* **2009**, *21*, 721.

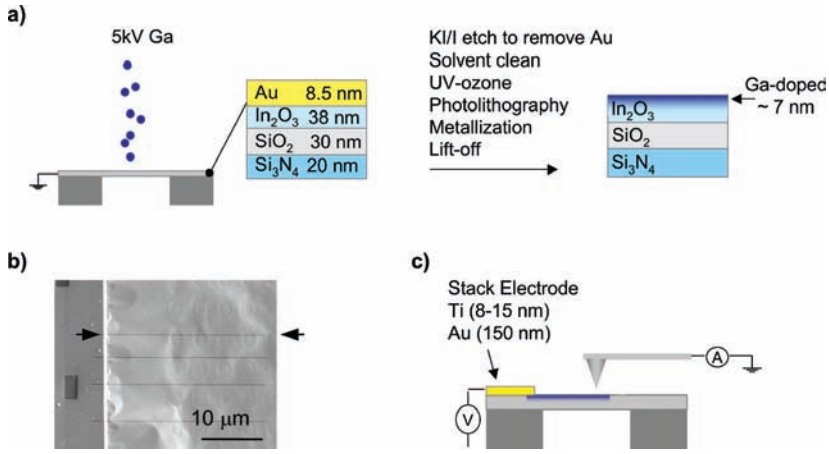


***Figure 2.*** Fabrication and characterization of nanowires. (a) FIB implantation directly onto ~96 nm thick suspended $Si_3N_4/SiO_2/In_2O_3$ film (cross-section of membrane layers is shown) at 5 kV. Au anticharging layer is removed immediately after fabrication. A cross-section schematic of the layered structure postdoping is shown on the right. (b) SEM image (top view) immediately after implantation showing FIB wires written at the edge of one window (arrows flank one wire). Although some film corrugation is observable, it does not interfere with AFM scanning or TEM imaging. (c) Schematic of the conductive AFM setup for collection of current maps.

## 2. Microstructure Background

To provide context for the discussion of potential doping mechanisms, a background on the relevant microstructure is first provided. $In_2O_3$ has a cubic crystal structure, and whereas the fully stoichiometric material is insulating,[44] introduction of substitutional dopants or creation of oxygen vacancies generates charge carriers, and the material becomes an n-type conductor while retaining its optical transparency. Detailed single-crystal X-ray diffraction studies reveal that $In_2O_3$ has a cubic bixbyite structure, also known as the C-type rare-earth sesquioxide structure. The body-centered unit cell has 80 atoms with a lattice parameter of 10.117 Å.[45] The crystal structure can be visualized by removing one-fourth of the anion lattice sites of the $2 \times 2 \times 2$ fluorite superstructure; these bixbyite empty anion (oxygen) sites are referred to as *structural* anion vacancies. The 48 lattice oxygen atoms are found in the *e* sites, and the 16 structural vacancies at *c* sites.

It is generally accepted that charge carrier generation in undoped $In_2O_3$ involves oxygen vacancies.[25,44] However, recent first-principles computational studies[46−50] suggest that interstitial In is responsible for the intrinsic conductivity of $In_2O_3$. These results argue that In interstitials generate shallower donor levels than those created by oxygen vacancies and that even shallower levels are formed when the interstitial In ions form complexes with the oxygen vacancies.[47] Another group[50] has proposed that persistent photoconductivity, resulting from oxygen vacancy defect states within the conduction band, leads to the observed free carriers in undoped $In_2O_3$. In addition, recent experimental studies of $O_2$ partial pressure effects on pure and doped $In_2O_3$ suggest yet another possible intrinsic defect cluster:[51] a singly positively charged cluster composed of both interstitial In and O. Despite the complexities arising from the rich chemistry of $In_2O_3$, the general consensus is that nonstoichiometry and crystal defects lead to charge carrier generation and that the intrinsic behavior of this oxide is n-type, i.e., electrons are the majority charge carriers.

With the above considerations in mind, detailed microstructural information on the FIB-derived nanowires was acquired by TEM techniques. Specifically, the STEM mode was combined with EDXS and EELS to acquire spatially resolved chemical information. These combined techniques provide chemical information images at the nanometer to atomic scale. For example, such instrumentation has been used to image single Sb dopant atoms in Si,[52] to decipher the atomic structure of complex oxides such as the high temperature superconductor YBCO[53] and to map $sp^2$ and $sp^3$ C atoms at diamond-Si interfaces,[54] thus providing an incisive tool for understanding structure−property relationships in nanomaterials. Here we employ it to analyze the spatial extent of Ga doping in the patterned $In_2O_3$ substrates and to examine Ga implantation-induced nanochemical changes, particularly at the host oxygen sites.

## 3. Experimental Section

**3.1. TEM Sample Preparation.** Because the aim here is to study implantation-induced phenomena, an important goal was to create TEM samples without resorting to traditional sputtering or ion milling-based thinning techniques. Rather, the present TEM-transparent samples were prepared by depositing $In_2O_3$ films directly onto specialty TEM grids (4107SN-BA, SPI Supplies, Inc.) having a 20 nm thick $Si_3N_4$ membrane suspended over 100 $\mu$m windows. Film depositions were carried out with a horizontal dual-gun ion-assisted deposition (HDG-IAD) system at room temperature, to deposit 30 nm of silica (99.99% target from Williams Advanced Materials), followed by 38 nm of highly resistive $In_2O_3$ (99.99% target from Williams Advanced Materials). More details can be found in Supporting Information.

**3.2. Ion Implantation.** Immediately following a 5 min UV-ozone treatment, 8.5 nm of Au was sputtered onto the suspended

(44) Bender, M.; Katasarakis, N.; Gagaoudakis, E.; Hourdakis, E.; Douloufakis, E.; Cimalla, V. *J. Appl. Phys.* **2001**, *90*, 5382.
(45) Marezio, M. *Acta Crystallogr.* **1966**, *20*, 723.
(46) Warschkow, O.; Ellis, D. E.; Gonzalez, G. B.; Mason, T. O. *J. Am. Chem. Soc.* **2003**, *86*, 1700.
(47) Tomita, T.; Yamashita, K.; Hayafuji, Y.; Adachi, H. *Appl. Phys. Lett.* **2005**, *87*, 3.
(48) Tanaka, I.; Tatsumi, K.; Nakano, M.; Adachi, H.; Oba, F. *J. Am. Ceram. Soc.* **2002**, *85*, 68.
(49) Mryasov, O. N.; Freeman, A. J. *Phys. Rev. B* **2001**, 64.
(50) Lany, S.; Zunger, A. *Phys. Rev. Lett.* **2007**, 98.
(51) Ohya, Y.; Yamamoto, T.; Ban, T. *J. Am. Ceram. Soc.* **2008**, *91*, 240.
(52) Voyles, P. M.; Muller, D. A.; Grazul, J. L.; Citrin, P. H.; Gossmann, H. J. L. *Nature* **2002**, *416*, 826.
(53) Klie, R. F.; Zhao, Y.; Yang, G.; Zhu, Y. M. *Micron* **2008**, *39*, 723.
(54) Muller, D. A.; Tzou, Y.; Raj, R.; Silcox, J. *Nature* **1993**, *366*, 725.

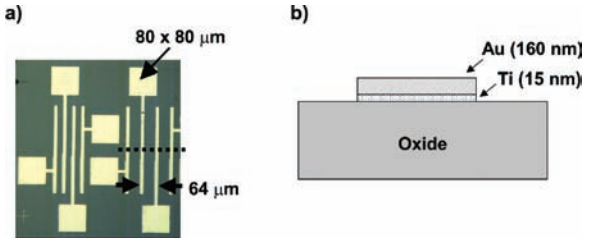


***Figure 3.*** Single nanowire current−voltage data collection. (a) Four-point probe electrode configuration. A representative location of the FIB-doped nanowires is indicated with a dashed line. (b) Stacked Ti/Au electrodes deposited on top of the doped nanowires were used to collect current−voltage curves from single nanowires.

oxide films. A dual-beam FEI NanoLab 600 FIB was used to perform Ga implantations (Figure 2a) at beam settings of 5 kV with a 1.6 pA beam current for an estimated surface dose of $4 \times 10^{16}$ ions $cm^{-2}$. Simultaneous Ga ion beam and electron beam operation is an essential detail because it allows imaging to be performed without unintentional implantation. Following FIB fabrication, the Au layer was removed with $KI/I_2$ aqueous solution (Transene Company, Inc.).

Secondary electron microscopy (SEM) images (Figure 2b) acquired immediately following ion implantation proved to be extremely useful for relocation purposes since the doped regions are not easily discernible except by conductive atomic force microscopy (cAFM). The FIB-doped nanowires were then electrically grounded by depositing AuPd alloy or Ti/Au stack electrodes at one terminus via photolithographic lift-off techniques (Figure 2c). The film corrugation, which can be discerned in Figure 2b, introduces some experimental complexity in the photolithographic processing; however, it is an essential step because TEM imaging requires the wires to be grounded in order to avoid severe damage through electrical charging. See Supporting Information for further details.

**3.3. TEM Imaging and Other TEM-Based Techniques.** All TEM imaging was performed using a JEOL 2100F Schottky field emission gun TEM operated at 200 kV in either conventional or scanning TEM modes. The membrane corrugation introduced some difficulty in STEM imaging because it led to changes in working distance, and it was thus necessary to regularly perform Ronchigram readjustment[55] when the beam traveled more than a few hundred nanometers. The energy loss near-edge spectra (ELNES) from both doped and undoped regions were collected using the Gatan imaging filter system, in the STEM mode. The energy loss spectra were collected using an energy resolution of 1.0 eV estimated from the full-width at half-maximum of the zero loss peak.

**3.4. Electrical Characterization.** Electrical measurements were carried out with a 4-point AuPd alloy electrode configuration deposited via shadow mask onto the nanowires fabricated on TCO films deposited on glass substrates (Figure 3). Multiple electrode spacings were fabricated and used to verify the independence of the nanowire conductivity as a function of nanowire length. Voltage ranges of ±5−10 mV were used to collect current−voltage curves with a Keithley 2400 sourcemeter. Rapid thermal anneals were carried out on nanowires fabricated on thin films on glass substrates (not TEM grids) with a RTP-600S (Modular Process Technology Corp.) instrument at 955 °C (0.5 $T_m$). Conductive AFM scanning was performed following annealing treatments to analyze annealing effects on the electrical contrast. The metal stacks used were either Ti/Au (15 nm/160 nm) or PdAu (160 nm) alloy.

## 4. Results

**4.1. TEM Imaging.** To assay the $In_2O_3$ microstructural changes induced by Ga implantation, TEM imaging was performed directly on stacked films (Figure 2a). Nanowires were imaged by TEM to define their crystalline and nanochemical properties. Figure 4a shows a typical STEM image. Here, contrast principally arises from differences in atomic mass, with negligible contribution from diffraction or crystal structure. Since STEM contrast from heavier elements is brighter while lighter elements appear darker, STEM images provide a chemical map. Furthermore, the beam is a mobile probe that allows local interrogation using spectroscopic techniques. The STEM mode was used here to aid in measuring the electrically active width by spatially mapping the Ga dopant distribution within the host oxide.

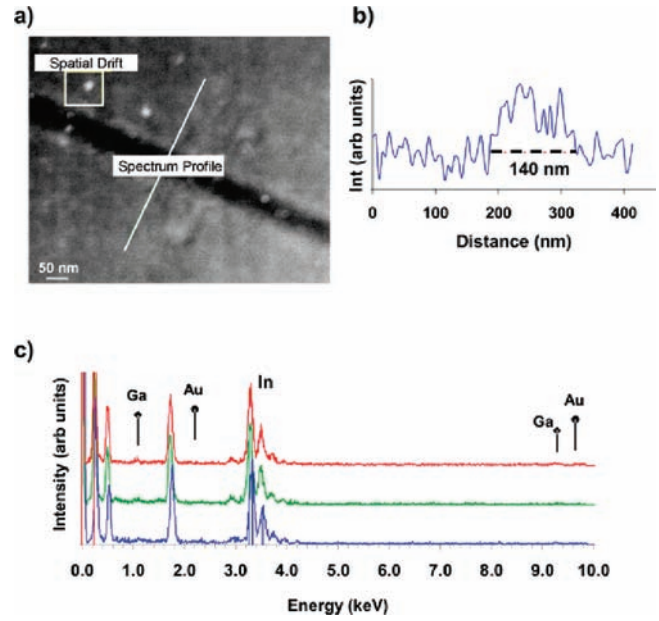


***Figure 4.*** TEM imaging and spatial chemical analysis of Ga-doped/patterned $In_2O_3$ films. (a) STEM image of a FIB-derived nanowire. (b) EDXS Ga $L_\alpha$ profile from the white line in part a. (c) Three representative EDXS spectra collected within the FIB-doped wire. Note the absence of a Au signal at the three major Au peaks (2.20, 2.29, and 9.71 keV).

A Ga EDXS profile (Figure 4b) was collected over the white line in Figure 4a, sampling ~420 nm of both doped and undoped oxide with 80 evenly spaced data points (1 nm beam). The signal-to-noise ratio is modest due to the small dimensions of the nanowire (3−7 nm deep by SIMS[43]) and the electron probe (1 nm). Nevertheless, the increased Ga $L_\alpha$ feature intensity in the doped regions is clearly evident. When quantified from the profile EDXS spectra (Figure 4b), the FIB-doped nanowire has a chemical width of ~140 nm. For completeness, the full EDXS spectrum is shown in Figure 4c and will be discussed in more detail in Section 4.3 below.

When imaged in the bright-field TEM mode, the wires afford very low contrast (Figure 5a). Consequently, the image was enhanced by increasing the digital contrast via a standard graphics program to better define the wire in Figure 5a (flanked by arrows). Using a 100 nm beam, diffraction patterns were collected from both the doped and undoped areas (Figure 5b and c, respectively). The undoped regions are clearly polycrystalline as indicated by the diffraction spots within the ring. In marked contrast, although faint remnants of one ring are present, the Ga-doped region shows almost completely amorphous character. The lack of a discernible crystal structure within the doped area indicates the microstructural disorder induced by the FIB implantation.

(55) Sigle, W. *Annu. Rev. Mater. Res.* **2005**, *35*, 239.

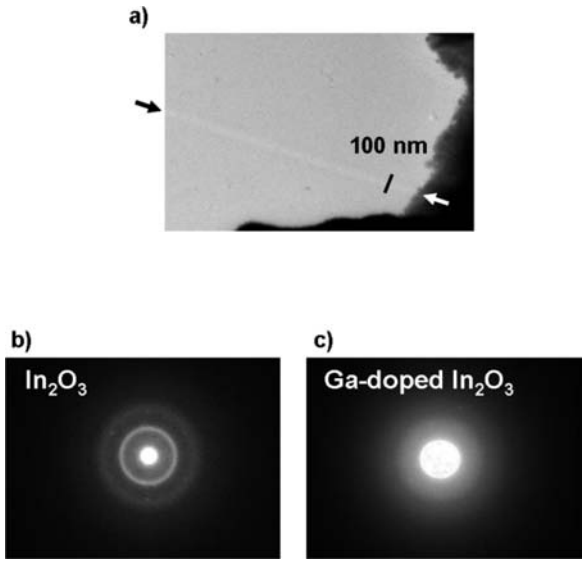


***Figure 5.*** Bright-field (BF) TEM imaging of Ga-doped/patterned $In_2O_3$ films. (a) BF TEM image of the FIB-doped wire. Arrows enclose the wire, and the scale bar is shown across the wire. The image contrast and brightness were increased to better visualize the FIB wire. (b) Nanodiffraction pattern taken with a ~100 nm beam from the undoped $In_2O_3$ region. Film polycrystallinity is evident from the presence of faint diffraction spots along the outer ring. (c) Nanodiffraction pattern from the FIB-doped wire shows that this area has been amorphized by the implantation cascade.

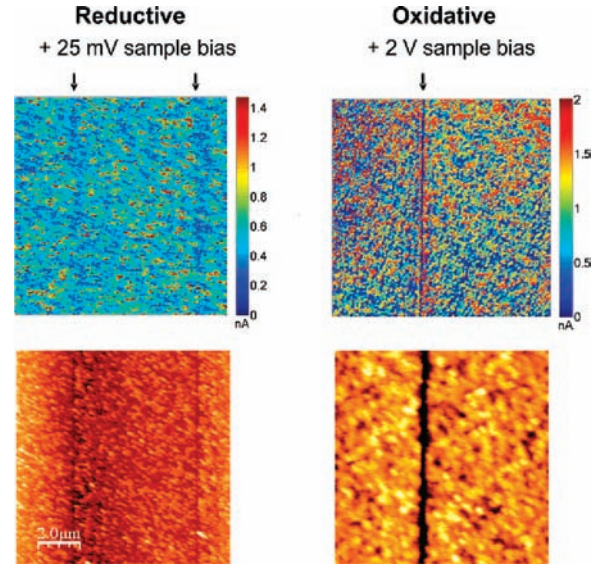


***Figure 6.*** Effect of RTA treaments on Ga-doped/patterned $In_2O_3$ films. Conductive AFM current maps (top) and topography (bottom) after RTA. Arrows point to the nanowires. A reductive atmosphere ($N_2$) during RTA essentially erases the FIB-patterned nanowire while increasing the entire film conductivity as evidenced by the low bias necessary to obtain ~0.5 nA average current across the image. An oxidative atmosphere also erases the FIB-patterned nanowires by lowering the nanowire conductivity as evidenced by the higher bias necessary to obtain a similar current scale as the reductive treatment.

**4.2. Annealing Experiments.** The hypothesis of disorder-induced doping via oxygen vacancies was tested by annealing the patterned films in both reducing and oxidizing environments. Reductive anneals of n-type TCOs typically aid carrier generation,[56,57] whereas the opposite behavior is observed for oxidizing anneals. Indeed, conductivity can typically be cycled with oxidative/reductive cycles,[57] and rapid thermal annealing (RTA) has been used to modify TCO electrical properties.[58−60] Figure 6 shows current and topography AFM maps of FIB-doped nanowires after reductive and oxidative RTA (the images are of wires created on thin blanket films and not on TEM suspended membranes). Here, RTA treatments (15 s) in flowing $N_{2(g)}$ increase the conductivity of the entire surface, as indicated in the cAFM current maps, to the extent that a 25 mV sample bias induces substantial tip−sample current flow. The reductive RTA effectively "erases" the contrast created by the doping. In marked contrast, RTA treatments under oxidizing conditions result in greatly decreased wire conductance to a level similar to that of the background. A substantial decrease in conductivity is observed as indicated by the higher bias necessary to achieve a similar electrical current scale as achieved following reductive RTA.

**4.3. Nanoscale Chemical Analysis.** In our preliminary report, SIMS depth-profiling revealed negligible Au content (which might arise from the Au anticharging layer) on either the surface or within the Ga-doped regions.[43] Thus, Au was eliminated as a potential source of increased conductance in doped regions. In the present study, we address this concern in greater depth.

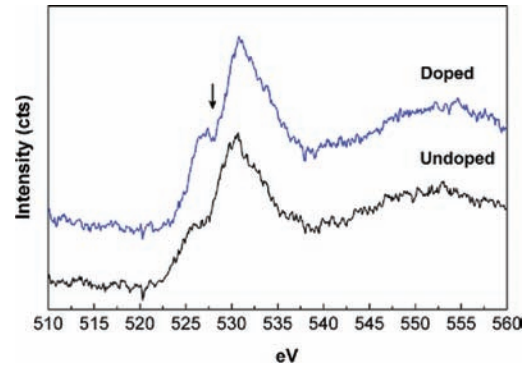


***Figure 7.*** Representative EELS oxygen edge spectra from Ga-doped and undoped regions of $In_2O_3$ films collected in STEM mode. Eight equally separated (10 nm) measurements were carried out in the profile mode over doped and undoped material. The pre-edge "dip" feature noted by the arrow is associated with changes in the chemical environment around the oxygen sites, either as oxygen vacancies or oxygen interstitials.

Full EDXS profiles were simultaneously collected during the Ga profiling so that Au signals could be analyzed across the nanowires. Figure 4c shows three full EDXS profiles taken at different positions within the FIB-doped wire. Clearly none of the three major Au peaks (2.20, 2.29, and 9.7 keV, all of similar expected intensities) are detected in the EDXS spectra taken within the FIB-doped areas (Figure 4c).

Spatially resolved chemical imaging was performed employing incoherent Z-contrast (Z = atomic number) techniques using a high-angle annular dark field (HAADF) detector. Figure 7 shows representative results for both FIB-implanted and non-implanted areas probed with EELS. The prominent difference between the two regions is the feature preceding the oxygen *K*-edge (O *K*-edge) seen in the doped spectrum. Transition metal oxide oxygen EELS spectra typically show only a single edge and have been thoroughly studied, particularly for transition

(56) Cava, R. J.; Phillips, J. M.; Kwo, J.; Thomas, G. A.; Vandover, R. B.; Carter, S. A.; Krajewski, J. J.; Peck, W. F.; Marshall, J. H.; Rapkine, D. H. *Appl. Phys. Lett.* **1994**, *64*, 2071.
(57) Hwang, J. H.; Edwards, D. D.; Kammler, D. R.; Mason, T. O. *Solid State Ionics* **2000**, *129*, 135.
(58) Kim, J. H.; Du Ahn, B.; Lee, C. H.; Jeon, K. A.; Kang, H. S.; Lee, S. Y. *J. Appl. Phys.* **2006**, 100.
(59) Ma, T. Y.; Shim, D. K. *Thin Solid Films* **2002**, *410*, 8.
(60) Weijtens, C. H. L. *J. Electrochem. Soc.* **1991**, *138*, 3432.

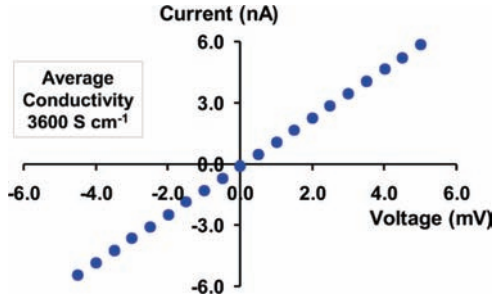


***Figure 8.*** Current−voltage characteristics of a single Ga-doped/patterned $In_2O_3$ nanowire. The inverse of the slope is $\sim 10^6$ Ω (with an $R^2$ fit of 0.9988 using linear regression). The average conductivity value given in the inset is taken from multiple measurements of two wires prepared on separate days and samples. For the data displayed in this figure, the wire dimensions were 110 nm wide, 3.1 nm deep, and 120 $\mu$m long.

metal oxides. The O *K*-edge typically has a step-like, abrupt onset at 532 eV and is strong in intensity and rich in features indicative of the chemical environment.[61] Energy-loss near-edge structure (ELNES) is also evident in the present spectra for doped and undoped sample regions (Figure 7). For the FIB-doped regions, 7 out of 8 spectra collected exhibit the pre-edge "dip" feature at 527 eV. In the undoped material, however, the EELS spectra exhibit either an inclined slope over this 525−528 eV range (6 out of 8 spectra) or zero slope (2 out of 8 spectra).

**4.4. Nanowire Electrical Characterization.** The electrical conductivity of the Ga-doped/patterned $In_2O_3$ nanowires was measured using a 4-point probe configuration. Figure 8 shows a representative current−voltage plot obtained from a single nanowire, which exhibits linear, ohmic behavior. An estimate of the conductivity ($\sigma$) can be extracted using the formula $\sigma = l/(RA)$, where $l$ is the wire length (electrode separation =120 $\mu$m for the current−voltage curve in Figure 8), $R$ the resistance (inverse of the current−voltage curve slope), and $A$ is the wire cross-sectional area. Defining the cross-sectional area of a wire resulting from implantation is challenging because the dopant distribution is not a step profile, i.e., the boundary between doped and undoped material is not atomically abrupt. Rather, the distribution has an approximately exponential decay with most of the dopants concentrated within 5 nm of the oxide surface, with no detectable Ga beyond 7 nm as reported in ref 43. Therefore, to estimate the conductivity, the total Ga depth was approximated by assuming a step-like profile having the same area as the area under the experimental dopant profile curve, which yields an approximate dopant depth of 3.1 nm. Using this estimate, the average wire conductivity is ~3600 S $cm^{-1}$. More conservatively, if the vertical dimension of the wire is assumed to be the depth for which the dopant SIMS signal drops to undetectable levels (~7 nm), then a lower bound conductivity estimate of 1600 S $cm^{-1}$ is calculated.

## 5. Discussion

For in-depth microstructural studies, TEM-ready samples were prepared using specialty grids (see Experimental Section for details). This preparative scheme provides unaltered nanowires that can be scanned directly by AFM and subsequently imaged with TEM. Thus, identical wires can be characterized in terms of their chemical, microstructural, and electrical properties. Nanoscale chemical investigations provide information on the spatial precision of this doping/patterning technique. Using the STEM mode, chemical image maps are readily acquired and the lateral extent of Ga doping is directly imaged. Spatially resolved chemical imaging was performed employing incoherent Z-contrast techniques[39,41] using a JEOL 2100F instrument and high-angle annular dark field (HAADF) detector. Here, image contrast is approximately proportional to $Z^n$, where the constant $n$ depends on the collection angle, $0.6 < n < 2$.[61] Sharp contrast is noted between the doped and undoped areas, underscoring the excellent spatial control achieved in the FIB Ga doping.

When the electron probe is controlled to scan across a single nanowire while simultaneously collecting the EDXS signal, further chemical details on the Ga content/distribution are acquired. The Ga EDXS $L_\alpha$ (1.098 keV) peak was chosen because it is strong and well-isolated from other signals. While the signal intensity is only ~3 times that of background due to the extremely small volumes probed, it is nevertheless clear that this technique can quantify the lateral Ga distribution (Figure 4b). The chemical nanowire width measured in the profile shown is ~140 nm. However, this measured width is broadened to a degree due to electron scattering, which is a function of sample thickness,[55] i.e., volume sampling effects must be taken into account. Nevertheless, note that the conductive AFM-derived width is in good agreement (cAFM width =160 nm when averaged over 1 $\mu$m of nanowire length). There are two potential sources of this modest discrepancy. In STEM imaging, a chemical signal is used to define the nanowire line width, whereas in cAFM, the electrical current flow between the tip and sample is used to define the line width. Any discrepancy could be due to oxygen vacancy formation, which in principle could exist at distances greater than the Ga implantation sites. Furthermore, tip broadening effects can be non-negligible in SPM since the effective tip radius affects achievable resolution. For example, note the higher resolution image in Figure 1. While the total ion dose here is 3 times greater than that yielding 160 nm wide wires, the derived nanowire width is closer to that from the STEM EDX Ga chemical profile.

Additional chemical EDXS analysis yields important information about the presence or absence of possible electrically active Au contaminants. For maximum resolution, the FIB implantation technique requires an anticharging layer, for which we chose Au since it can be easily removed without using acidic etchants. Whether Au might be unintentionally incorporated via knock-on implantation during FIB processing is a valid concern. In the initial study,[43] the Au ion peak was monitored throughout the SIMS depth-profiling experiments, where sampling relatively large areas (28 $\mu$m × 28 $\mu$m) was necessary to achieve reasonable signal-to-noise ratios. Negligible Au peak counts were observed throughout SIMS data collection. Here, this issue is now addressed at the nanoscale. Figure 4c shows three representative EDXS spectra (out of several taken at various points within the doped $In_2O_3$) that confirm the absence of the three strongest Au EDXS peaks. Note that in the previous work, the Au SIMS peak was monitored simultaneously with depth profiling, whereas the signal in the present work is collected with a 1 nm electron beam that probes the entire sample thickness. Thus, the signal is of high lateral selectivity yet with full-depth range. The EDXS data unequivocally confirm the absence of Au from the FIB-doped regions and show that spurious coimplantation of Au during FIB implantation does not contribute to the increased conductivity achieved with the present fabrication technique.

(61) Egerton, R. F. *Electron Energy-Loss Spectroscopy in the Electron Microscope*; Plenum: New York, London, 1996.

In this study, STEM provides chemical contrast imaging while EDXS assays the lateral extent and location of Ga doping, while also confirming the absence of adventitious Au. As a complement, bright-field (BF) imaging and nanodiffraction provide information on microstructural changes resulting from the FIB patterning process with Ga. The image contrast in BF originates from both sample thickness and crystal structure in that thicker samples attenuate the intensity of the transmitted beam, and more crystalline materials have the same effect by diffracting a greater portion of the beam. Since it has been shown here that the FIB doping process leads to minimal topographic changes as assayed by AFM, the observed BF TEM contrast can be attributed to changes in $In_2O_3$ crystal structure, specifically amorphization of the doped portions of the film. Since the BF contrast is low at the boundary of the crystalline and amorphous oxide at higher magnifications, nanodiffraction patterns were collected. The polycrystalline nature of the undoped host oxide is clearly evident in Figure 5b, while Figure 5c readily confirms the lack of crystalline microstructure in the FIB-patterned/Ga-doped $In_2O_3$ regions. These diffraction patterns reveal the results of the collision cascade and provide direct assessment of disorder in the doped areas.

The self-doping[62] capacity of $In_2O_3$ can be described using Kröger−Vink notation, where the subscripts denote the site where the defect resides and superscripts denote defect charge as follows: ($^x$) neutral, ($^\bullet$) positive, and ($'$) negative charges (eq 1). Thus, oxygen vacancies in the bixbyite structure can be represented by eq 1, where each oxygen vacancy point defect donates two electrons to the conduction band.

$$O_0^x \rightarrow \frac{1}{2}O_{2(g)} + V_o^{\bullet\bullet} + 2e' \qquad (1)$$

To further scrutinize the possibility that increased conductivity of the doped regions arises from collision-created oxygen vacancies, annealing studies were performed. In particular, rapid thermal anneal (RTA) treatments were employed to avoid significant diffusion of Ga dopants or other potentially important chemical or ionic species. The observed trends are compelling and support the model that oxygen vacancies created via knock-on collision during implantation lead to increased local conductance in the Ga-doped oxide. These particular samples were intentionally prepared with a doping dose that induced sputtering, and therefore a trench is formed and is visible in the AFM images. This topographic feature confirms that while electrical properties are altered by the RTA, significant morphological changes do not occur. In particular, the trench created by the FIB remains intact following either reductive or oxidative RTA (Figure 6). Furthermore, in light of the cAFM data (pre- and post-RTA) coupled with the unlikelihood of oxide recrystallization under the RTA conditions employed, oxide amorphization does not appear to be a significant factor in the doping process, although it should not be surprising that an amorphous TOS/TCO has excellent transport properties (see more below). However, rigorous exclusion of interstitial oxygen as the origin of the significant doping-induced conductivity changes is not possible because of the presence of pre-edge features in the EELS oxygen spectra. As a final defect chemistry comment, note that acceptor-type doping can be ruled out here since $In_2O_3$ is a nonamphoteric[63] n-type conductor. Moreover, singly charged $Ga^+$ ions are not expected to be acceptor dopants because ionic compensation in this oxide would nullify this effect.[62]

In the present work, chemical contrast images are visualized in the STEM mode. As noted above, Z-contrast images are collected using HAADF detection, which preserves the unperturbed energy-loss spectrum (as well as energy dispersive X-ray collection). The combination of Z-contrast imaging (structure + composition) and EELS (composition + bonding characteristics) affords direct, nanoscale chemical characterization of the FIB-doped and undoped oxide regions. In particular, EELS spectroscopy probes the local density of unoccupied states. In this investigation, the central points of interest are the core-loss energies corresponding to the oxygen chemical environment, namely, the O *K*-edge. The EELS O absorption *K*-edge originates from transitions from the O *K*-shell into unoccupied oxygen 2p states. Thus, EELS spectroscopy is ideal for characterizing metal oxides, and many systems have been studied including $SnO_2$ comparisons to $SiO_2$,[64] $LaCoO_3$ and $YB_2Cu_3O_7$,[53] $SrTiO_3$,[65] Sn oxidation,[66,67] $PbTiO_3$,[68] $HfO_2$,[69] vanadium oxides,[70] niobium oxides,[71] $SrCoO_3$,[72] and Sn-doped $In_2O_3$.[73,74] The present "dip-like" pre-edge feature at 527 eV has been noted in other oxides. For example, Lin et al.[70] studied the O *K*-edges of $V_2O_5$, $VO_2$, and $V_2O_3$, which exhibit two oxygen pre-edge features. The intensity ratios of the first and second oxygen pre-edge peaks correlate with decreasing V oxidation state. Furthermore, $(VO)_2P_2O_7$ compounds were analyzed, and significant changes in the O *K*-edge can be assigned to d-p-$\sigma$ hybridization, with P $\sigma$ character contributing to the EELS features. In another study,[69] the Hf:Al ratio was varied in hafnium aluminate thin films, and it was found that Al addition to $HfO_2$ involves two intrinsic oxygen defects (vacancies and interstitials) found in the pure oxide. In a similar investigation, analogous oxygen pre-edge features were reported in monoclinic $HfO_2$ upon Y and Al incorporation[61] and were attributed to defect-induced densities of states.[75] EELS studies of superconducting oxides routinely identify pre-edge features at the oxygen edge[76] that are associated with oxygen-centered holes. Importantly, while EELS detects changes in oxygen chemical environment leading to carriers, the relative importance of oxygen vacancies versus interstitials cannot be unambiguously assayed.

(62) Mason, T. O.; Gonzalez, G. B.; Kammler, D. R.; Mansourian-Hadavi, N.; Ingram, B. J. *Thin Solid Films* **2002**, *411*, 106.
(63) Sheets, W. C.; Mugnier, E.; Barnabe, A.; Marks, T. J.; Poeppelmeier, K. R. *Chem. Mater.* **2006**, *18*, 7.
(64) Jimenez, V. M.; Mejias, J. A.; Espinos, J. P.; GonzalezElipe, A. R. *Surf. Sci.* **1996**, *366*, 545.
(65) Klie, R. F.; Zhu, Y. *Micron* **2005**, *36*, 219.
(66) Hoflund, G. B.; Corallo, G. R. *Phys. Rev. B* **1992**, *46*, 7110.
(67) Bevolo, A. J.; Verhoeven, J. D.; Noack, M. *Surf. Sci.* **1983**, *134*, 499.
(68) Fu, L. F.; Welz, S. J.; Browning, N. D.; Kurasawa, M.; McIntyre, P. C. *Appl. Phys. Lett.* **2005**, 87.
(69) Li, Q.; Koo, K. M.; Lau, W. M.; Lee, P. F.; Dai, J. Y.; Hou, Z. F.; Gong, X. G. *Appl. Phys. Lett.* **2006**, 88.
(70) Lin, X. W.; Wang, Y. Y.; Dravid, V. P.; Michalakos, P. M.; Kung, M. C. *Phys. Rev. B* **1993**, *47*, 3477.
(71) Bach, D.; Stormer, H.; Schneider, R.; Gerthsen, D.; Verbeeck, J. *Microsc. Microanal.* **2006**, *12*, 416.
(72) Stemmer, S.; Sane, A.; Browning, N. D.; Mazanec, T. J. *Solid State Ionics* **2000**, *130*, 71.
(73) Morikawa, H.; Kurata, H.; Fujita, M. *J. Electron Microsc.* **2000**, *49*, 67.
(74) Zhu, F. R.; Huan, C. H. A.; Zhang, K. R.; Wee, A. T. S. *Thin Solid Films* **2000**, *359*, 244.
(75) Wang, X. F.; Li, Q.; Moreno, M. S. *J. Appl. Phys.* **2008**, *104*, 1.
(76) Zhang, H.; Dravid, V. P. *J. Am. Ceram. Soc.* **1993**, *76*, 1143.

Other EELS differences not observed here are O *K*-edge onset shifts. Such shifts would denote a change in binding energy, indicative of oxygen bonding changes. Another potential difference not observed is the presence of double peaks in the O *K*-edge energy loss region; this feature is typically seen in transition metal oxides having hybridization of O 2p orbitals with metal 3d orbitals.[53,70,77] This EELS feature is useful in determining the metal coordination environment, specifically when multiple oxidation states are present.

In terms of EELS information about Ga dopants, the only region accessible to the present study is the $M_{2,3}$ edge at 103 eV. This edge has a delayed maximum and detectable intensity but cannot provide Ga oxidation state information since the two transitions yielding 3p shell information ($M_2$ and $M_3$) overlap. Oxidation state is typically extracted by analysis of changes in the $X_2$:$X_3$ ratio where X represents an electronic shell. This situation may partially explain the paucity of Ga EELS valence spectroscopy literature. For this information to be properly collected and analyzed, diverse reference samples having known Ga oxidation states are required, and the chemical state of each confirmed via other techniques. This effort is beyond the scope of the present study. No other prominent differences are noted when the full EELS spectra are carefully analyzed.

The 4-point probe current−voltage data coupled with the measured nanowire dimensions allow the electrical conductivity to be estimated. The average nanowire conductivity is found to be ∼1600−3600 S cm$^{-1}$. Ga-doped $In_2O_3$ thin films grown by conventional methods exhibit similar or somewhat lower conductivities (up to 1700 S cm$^{-1}$),[78−81] demonstrating the effectiveness of FIB in forming highly conductive, optically transparent nanowires. During implantation, the collision cascade creates lattice damage, knocking oxygen atoms out of their lattice positions and leading to oxygen vacancies and interstitials. The self-doping[62] capacity of $In_2O_3$ is well-known, with each oxygen vacancy point defect resulting in donation of two electrons to the conduction band. Recent first-principles electronic structure calculations suggest the possibility of oxygen interstitials forming shallow donor levels, and thus oxygen interstitials may also create carriers via this mechanism. Alternatively, it is also plausible that the amorphization of the oxide structure could contribute to the significant conductivity. Amorphous TCO systems are becoming increasingly common,[82−88] examples of which include $In_{0.8}Zn_{0.2}O_y$,[89] which exhibits conductivity in the $3 \times 10^3$ S cm$^{-1}$ range.[89,90] While little is known about dimensionality effects on transport in amorphous nanowires,[91] the fact that the conductivity of the present materials is comparable to that of typical bulk Ga-doped $In_2O_3$ thin films argues that the effects may not be large. Note, however, that little is also known about amorphous Ga-doped $In_2O_3$ films, and the aforementioned data are for polycrystalline films.

## 6. Conclusions

We have quantitatively characterized the chemical, microstructural, and electronic properties of novel, Ga FIB-derived $In_2O_3$ TCO nanowires. A methodology for preparing TEM-ready samples is presented that enables detailed TEM-based analysis of individual nanowires. Differences in diffraction features between doped and undoped oxide regions, accompanied by RTA results, support a model in which oxygen vacancies and amorphization comprise the predominant doping/carrier creation mechanism in this system. The same isolated nanowires were subjected to chemical profiling, providing quantitative information on the lateral Ga doping dimensions, which are in good agreement with cAFM imaging results. Furthermore, spatially selective nanoscale EELS spectroscopy provides additional evidence for changes in the oxygen site chemical environment in the FIB-processed/doped $In_2O_3$, and of negligible changes in the surrounding non-FIB-processed/undoped oxide. Note also that the conductivity of the present nanowires, ∼1600−3600 S cm$^{-1}$, is a respectable TCO charge transport metric and falls within the range for conventionally grown Ga-doped $In_2O_3$ thin films. This high conductivity coupled with FIB direct write flexibility presents a promising strategy for implementing transparent conducting interconnects in invisible integrated circuitry.

**Acknowledgment.** This work was supported by the Northwestern University MRSEC (NSF DMR-0520513), the Army Research Office (ARO W911NF-05-1-0177), the Department of Energy (DE-FG02-06ER46320), and the National Science Foundation (NSF ECS-0609064). FIB and TEM experiments were performed in the EPIC facility of the NUANCE Center at Northwestern University. NUANCE is supported by the NSF-NSEC, NSF-MRSEC, Keck Foundation, State of Illinois, and Northwestern University. N.E.S. acknowledges IBM for a predoctoral fellowship.

**Supporting Information Available:** Experimental procedures for sample preparation, ion implantation, TEM imaging, and electrical characterization. This material is available free of charge via the Internet at http://pubs.acs.org.

JA9092242

(77) Degroot, F. M. F.; Grioni, M.; Fuggle, J. C.; Ghijsen, J.; Sawatzky, G. A.; Petersen, H. *Phys. Rev. B* **1989**, *40*, 5715.
(78) Minami, T. *J. Vac. Sci. Technol., A* **1999**, *17*, 1765.
(79) Minami, T. *Mater. Res. Soc. Bull.* **2000**, *25*, 38.
(80) Wang, A. C.; Edleman, N. L.; Babcock, J. R.; Marks, T. J.; Lane, M. A.; Brazis, P. R.; Kannewurf, C. R. *J. Mater. Res.* **2002**, *17*, 3155.
(81) Phillips, J. M.; Kwo, J.; Thomas, G. A.; Carter, S. A.; Cava, R. J.; Hou, S. Y.; Krajewski, J. J.; Marshall, J. H.; Peck, W. F.; Rapkine, D. H.; Vandover, R. B. *Appl. Phys. Lett.* **1994**, *65*, 115.
(82) Jeong, S.; Ha, Y. G.; Moon, J.; Facchetti, A.; Marks, T. J. *Adv. Mater.* **2010**, *22*, 1346.
(83) Walsh, A.; Da Silva, J. L. F.; Wei, S. H. *Chem. Mater.* **2009**, *21*, 5119.
(84) Perkins, J. D.; van Hest, M.; Teplin, C. W.; Alleman, J. L.; Dabney, M. S.; Gedvilas, L. M.; Keyes, B. M.; To, B.; Ginley, D. S.; Taylor, M. P.; Readey, D. W. *Conference Record of the 2006 IEEE 4th World Conference on Photovoltaic Energy Conversion*; IEEE: New York, 2006; Vol.s *1 and 2*, p 202.
(85) Buchholz, D. B.; Liu, J.; Marks, T. J.; Zhang, M.; Chang, R. P. H. *ACS Appl. Mater. Interface* **2009**, *1*, 2147.
(86) Kim, D.; Koo, C. Y.; Song, K.; Jeong, Y.; Moon, J. *Appl. Phys. Lett.* **2009**, 95.
(87) Kim, H. S.; Kim, M. G.; Ha, Y. Q.; Kanatzidis, M. G.; Marks, T. J.; Facchetti, A. *J. Am. Chem. Soc.* **2009**, *131*, 10826.
(88) Barquinha, P.; Pereira, L.; Goncalves, G.; Martins, R.; Kuscer, D.; Kosec, M.; Fortunato, E. *J. Electrochem. Soc.* **2009**, *156*, H824.
(89) Bellingham, J. R.; Phillips, W. A.; Adkins, C. J. *J. Phys.: Condens. Matter* **1990**, *2*, 6207.
(90) Narushima, S.; Orita, M.; Hosono, H. *Glass Sci. Technol.* **2002**, *75*, 48.
(91) For results on free-standing $In_2O_3$-based nanowires with much lower doping levels but high field-effect mobilities, see: (a) Chen, P.-C.; Shen, G.; Chen, H.; Ha, Y.-G.; Wu, C.; Sukcharoenchoke, S.; Fu, Y.; Liu, J.; Facchetti, A.; Marks, T. J.; Thompson, M. C.; Zhou, C. *ACS Nano* **2009**, *3*, 3383. and references therein. (b) Ju, S.; Ishikawa, F.; Chen, P.; Chang, H.-K.; Zhou, C.; Ha, Y.-G.; Liu, J.; Facchetti, A.; Marks, T. J.; Janes, D. B. *Appl. Phys. Lett.* **2008**, *92*, 222105-1. (c) Ju, S.; Facchetti, A.; Xuan, Y.; Liu, J.; Ishikawa, F.; Ye, P.; Zhou, C.; Marks, T. J.; Janes, D. B. *Nat. Nanotechnol.* **2007**, *2*, 378.